

Quasi-Geostrophic Flow over Anisotropic Topography

G.F. Carnevale

Scripps Institution of Oceanography, University of California, San Diego La Jolla, California 92093, USA

R. Purini

Istituto di Fisica dell'Atmosfera, P.le Luigi Sturzo 31, Roma, Italy

P. Orlandi and P. Cavazza

Dipartimento di Meccanica e Aeronautica, Università di Roma, "La Sapienza", Via Eudossiana 16, 00184 Roma, Italy

Abstract. The orientation of an anisotropic topographic feature in a large-scale flow will affect the vorticity production that results from the topography-flow interaction. This in turn affects the amount of form drag that the ambient flow experiences. For quasi-geostrophic flow over a hill with an elliptical cross section in the horizontal, it is shown that the strength of the form drag depends not only on the magnitude of the angle that the topographic axis makes to the oncoming stream, but also on the sign of that angle. For sufficiently low topography, it is found that a positive angle of attack leads to a stronger form drag than that obtained with the corresponding negative angle. For strong topography, this relation is reversed, with the negative angle then resulting in the stronger form drag.

Introduction

We explore how the local vorticity distribution over topography changes as a function of the orientation of the topography with respect to the ambient large-scale flow. Our original motivation in this line of inquiry stemmed from recent work showing that the Antarctic Circumpolar Current's strength is strongly affected by the underlying topography. The dynamical balance of the Antarctic Circumpolar Current has long been a mystery. Bottom friction and continental borders alone are insufficient to absorb the momentum input from wind forcing. The simulations of McWilliams, Holland and Chow (1978), Wolff and Olbers (1989) and Treguier and McWilliams (1990) have gone a long way toward proving the hypothesis that the input from wind stress is ultimately balanced through form stress involving submerged ridges. The ridges under the Antarctic Circumpolar Current are not oriented meridionally, perpendicular to the mean current, but rather are at oblique angles (e.g., Macquarie Ridge, South East Indian Ridge, Pacific Antarctic Ridge, etc.). Treguier and McWilliams (1990) included randomly generated topographies in their studies, and Wolff, Meier-Reimer, and Olbers (1991) included a realistic representation of the Macquarie Ridge Complex. Another reason for interest in the effects of changing the flow-topography orientation follows from the fact that local flow over topog-

raphy will depend on this orientation, and this local flow will be important in determining the distribution of temperature, nutrients and, hence, biology over the topography. For example, in the Southern California Bight there are several banks of elliptical shape (e.g., Nidever Bank). When the direction of the large-scale current in this region changes, one expects the current regime over the bank to change (including the distribution of the regions of strongest upwelling). The local flow then determines the distribution of plankton and predators over the bank (Genin 1987). Similar comments could be made about seamounts which have an elongated structure (e.g. Horizon Guyot) (cf. Genin, Noble and Lonsdale 1989).

The general question of large-scale flow over topography in a rotating environment has been subject to very intense investigation due to the many possible applications to both the atmosphere and the oceans. In particular, the flow over bottom irregularities such as seamounts is an important source of eddy variability in the oceans. Also, the interaction of the flow with the topography produces a reaction on the flow called form drag that can, in both atmospheric and oceanic applications, significantly retard or block the oncoming flow. Numerous studies of flow-topography interaction have been performed with analytical, numerical and laboratory methods. For purposes of analysis and intuitive understanding, many of these studies have focused on models using

isolated, circularly-symmetric hills. Excellent historical reviews of that work can be found in Huppert and Bryan (1976), Johnson (1978), Bannon (1980), and Verron and Le Provost (1985). For such simplified models, the question of orientation of the topography with respect to the flow does not come into question. However, those models point out a basic asymmetry of the flow over topography problem, in that vortex tube compression always produces an anticyclone above a hill and this advects the fluid around the hill in the anticyclonic direction. We will see below, that for non-circularly symmetric topographies, the basic asymmetry of the flow interacts with the asymmetry of the topography in a way that produces a dependence on the orientation of the topography for vorticity production and for form drag. Consider, for example, Figure 1. Two configurations are shown (from above) in which a large-scale flow crosses an elliptical topography. The situations look symmetric, but, in fact, the form drag is different in the two cases. This will be explained in detail below.

Of course, there are already many notable works that examine flow-topography interactions with a model of topography more complicated than the circularly symmetric hill. Merkin and Kalnay-Rivas (1976) consider an elliptical topography with two orientations, cross stream and along stream. Pierrehumbert and Malguzzi (1984) consider a dipolar topographic forcing (but with a single orientation). Cook and Held (1992) have investigated flow over an elliptical topography, with a single orientation, in a general circulation model. We should also note that there have been many excellent studies of flow over elongated topography in the form of ridges. In most cases, however, the ridge is of infinite extent and oriented perpendicular to the flow. An exception is the study by Boyer (1971) who considers flow over a ridge of infinite extent at an angle to the large-scale flow. This list of examples does not even begin to mention all of the studies with irregular or random topography or those with actual representations of features on the earth's surface. On the whole, however, there have not been any systematic studies of the effects of orientation of anisotropic topography of finite extent.

For flow in a rotating environment, the simplest model that captures the essential effects of vortex tube compression/stretching is the quasi-geostrophic model. Within the context of that model, in section 2, we set up the basic equations for the problem of determining how the local flow around the topography depends on the orientation of that topography

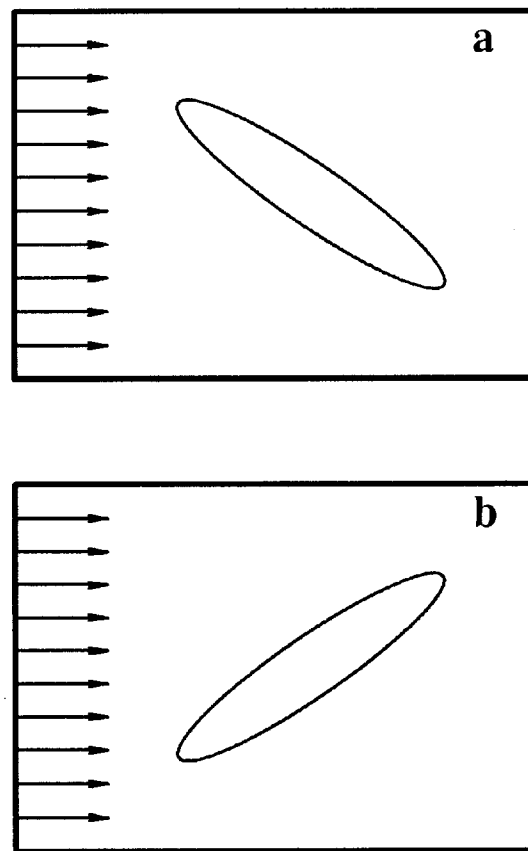


Figure 1. Schematic of large-scale flow over elliptical hills. In which case will the drag be greater, for the (a) positive angle of attack or for the (b) negative angle of attack?

with respect to the large-scale flow. In section 3, we give the results of simulations that show how the vorticity distribution over the topography depends on the orientation of that topography in the current. In section 4, we examine the dependence of the form drag on the topographic orientation, and relate the results to the vorticity distributions described previously in section 3. We develop the perturbation theory for the case of weak topography, and compare the predictions to results from the simulations. Furthermore, we present a simple point-vortex model that helps to explain the transition from the behavior of the form drag as a function of the angle of attack, as observed in the weak topographic regime, to the very different behavior observed in the strong topographic regime. This report is a greatly expanded version of Carnevale, Purini, Orlandi and Cavazza (1995).

The Model

The variation of the flow with topographic orientation is captured, in simplest form, by the quasi-geostrophic model for a single homogeneous layer under a rigid lid. For this model to be appropriate first requires that the rotation rate of the environment is sufficiently high so as to dominate local advective processes. The relative importance of rotation can be measured by the Rossby number, which is defined by

$$\epsilon = \frac{U}{fL}, \quad (1)$$

where L is a typical horizontal scale for the topography, f is the Coriolis parameter, which is twice the rotation rate, Ω , and U is the velocity of the oncoming stream. For ϵ sufficiently small, the flow will be in geostrophic balance, that is, the pressure force, including the centrifugal force, is balanced entirely by the Coriolis force in the momentum equation. Thus we have

$$2\Omega \times \mathbf{u} = -\frac{\nabla p}{\rho}, \quad (2)$$

where \mathbf{u} is the velocity of the flow and ρ is the fluid density, which we will assume is constant, and p is the thermodynamic pressure plus the potential for the centrifugal force. Taking Ω to be in the z -direction, we can write the components of the geostrophic flow as

$$u = -\frac{1}{f\rho} \frac{\partial p}{\partial y} \quad (3)$$

$$v = \frac{1}{f\rho} \frac{\partial p}{\partial x}, \quad (4)$$

in the x and y directions respectively, and the pressure is constant in the z -direction. Further, assuming that the rotation rate does not vary with position, and using incompressibility, it follows that if there is no flow through the upper surface, the flow is entirely two-dimensional (the Taylor-Proudman theorem). The streamfunction for this flow can be taken as proportional to the pressure:

$$\Psi = \frac{p}{f\rho}. \quad (5)$$

Furthermore, we assume that the layer thickness variation is a small fraction of the mean depth. The essence of the quasi-geostrophic model then is the horizontal advection of potential vorticity defined by

$$q = \nabla^2 \Psi + h. \quad (6)$$

h is the scaled topography given by $h = f\Delta H/H_0$, $-H_0$ is the average depth, and ΔH is the height of the bottom above the mean bottom level. Thus the quasi-geostrophic evolution equation is given by

$$\frac{\partial q}{\partial t} + J(\Psi, q) = -r\zeta + \nu \nabla^2 \zeta, \quad (7)$$

where J is the Jacobian defined as usual by

$$J(A, B) = A_x B_y - A_y B_x. \quad (8)$$

This is the simplest model which captures the effect of vortex tube stretching due to passage over topographic features. Besides the advection, we have also included two viscous effects: a bottom drag due to Ekman pumping, and a horizontal diffusion of relative vorticity. For a systematic derivation of the quasi-geostrophic evolution equation, see Pedlosky (1987).

We need to define a model of a confined asymmetric topography. The studies of Verron and Le Provost (1985) were performed with a Gaussian shaped topography, which in our notation would be

$$h(x, y) = h_0 e^{-(x^2+y^2)/R^2}, \quad (9)$$

with R a constant. As a simple generalization of this form to elongated structures, we take

$$h(x, y) = h_0 e^{-(x'^2/a^2 + y'^2/b^2)}, \quad (10)$$

where the coordinates x' and y' are just the old coordinates x and y rotated by the angle of attack of the topography with respect to the oncoming stream, as defined in Figure 2. Specifically

$$x' = x \cos \alpha - y \sin \alpha \quad (11)$$

$$y' = x \sin \alpha + y \cos \alpha, \quad (12)$$

where a and b define the major and minor axes of the contour of topography at the level with value $h(x, y) = e^{-1}$.

This topography is confined in the sense that its height a few lengths R from the origin is negligible for our purposes. This is the topography used for the discussion in the next two sections. It will be convenient to designate specific terms for the two ends of the ellipse representing the topography. Accordingly, the upstream end of the ellipse will be referred to as the nose of the topography, and the downstream end as the tail. Also we will refer to the line of highest points along vertical cross sections parallel to the minor axis as the crest of the topography.

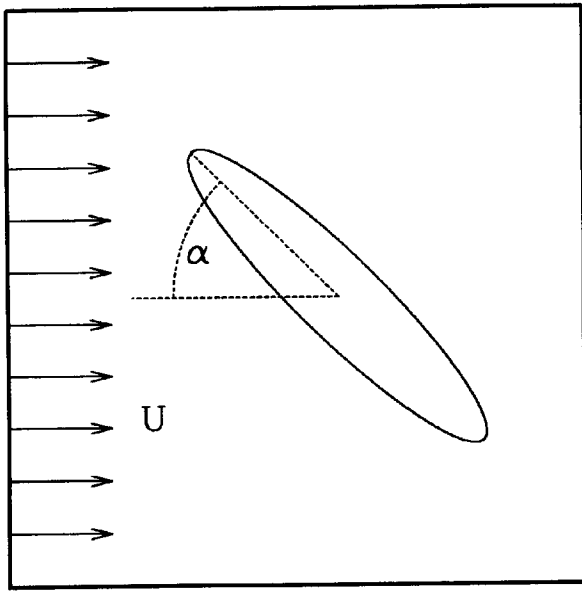


Figure 2. Schematic defining the angle of topographic orientation with respect to the flow. The scaled topographic height, defined in the text, is given by $h(x, y) = h_0 \exp(-x'^2/a^2 - y'^2/b^2)$, in coordinates x' and y' that are aligned with the topographic principal axes in a horizontal cross section. The lengths of the major and minor axes of the contour of topography at level $h(x, y) = e^{-1}$ are a and b . The angle of attack, α , is defined as the (counterclockwise) angle from the major axis to the axis of the large scale-flow. A positive angle of attack, $\alpha = 45^\circ$, is illustrated here.

Verron and Le Provost (1985) define a nondimensional parameter that measures the importance of topographic terms relative to the pure advective terms in equation (14). This parameter is given in our notation by

$$\mu = h_0 \frac{L}{U}, \quad (13)$$

where L is a typical horizontal length scale for both the topography and variations in the flow. Verron and Le Provost (1985) consider only the case of circularly symmetric topography in which our parameters a and b are both equal and take the value $\frac{1}{2}L$. For sufficiently small viscosity, Verron and Le Provost identified two distinct flow regimes separated by the critical value $\mu_d = 11$. When $\mu < \mu_d$, i.e. when the topography is 'weak' or the flow is strong, the flow is close to the inviscid solution given by $\zeta = -h$. For $\mu > \mu_d$, trapping of the positive vortex can occur, at least temporarily, forming a dipole, which is unstable in the purely inviscid case. Unless there is substan-

tial viscosity, the positive vortex is eventually shed downstream.

For our case, the definition of μ is somewhat ambiguous since there are now two length scales associated with the topography. In what follows, we have chosen to nondimensionalize all length scales by $L = 2a$ where a is the larger of a and b . Thus the length of the major axis is fixed at $a = 0.5$. We choose to fix the length of the minor axis at $b = 0.1$ as a representative value giving a topography which is far from circular but yet not in the realm of long thin bodies. Furthermore, we nondimensionalize time with the advective time scale, U/L . In all of the simulations with fixed, U , its value is taken to be 1, and so, the value of h_0 in these units is the same as μ .

As for the boundary conditions on the streamfunction Ψ , we consider the case in which the flow is uniform at infinity. Thus we can put $\Psi = \psi - Uy$, where the boundary conditions are that ψ vanishes at infinity. These boundary conditions present some difficulties in deciding on the appropriate numerical simulation scheme. From previous studies, we know that if we impulsively start a large-scale flow over a hill, the zero vorticity flow originally situated over the hill will be pushed off and become a cyclone, which may be completely or partially shed downstream. For our problem, we need to allow such shed vorticity to pass out of our limited computational domain. We have actually performed our simulations with three different codes with different boundary conditions to check that the effects discussed here are independent of the exact specifications of the boundaries. In one case, we have a finite difference code in a rectangular domain. Slip boundary conditions are used on the two walls aligned along the flow direction. The velocity on the inflow side of the channel is specified to be exactly U in the x -direction and zero in the y -direction. The outflow boundary has a radiation condition based on the Orlanski (1976) scheme. In the second case, we replaced equation (7) with the following

$$\frac{\partial q}{\partial t} + J(\psi - Uy, q) = -r\zeta + \nu \nabla^2 \zeta, \quad (14)$$

where we have explicitly introduced the decomposition $\Psi = \psi - Uy$. We solve this advection equation spectrally assuming ψ is periodic in both x and y directions. We used the dealiased pseudospectral method as described in Patterson and Orszag (1972). The problem of the shed vorticity is dealt with by adding to this code a physical space filter on the vorticity. Specifically, the local vorticity, ζ , is set equal

to zero every time step at all points beyond a certain radius, which is taken to be larger than L , the representative horizontal scale of the topography. In the third case, simulations were also performed with a doubly-periodic spectral code. Here the shed vorticity re-enters the domain, but when we are considering the long term limit, when all transients have died out, this does not adversely affect the results. All the results reported below were found for all three types of codes and thus appear, at least qualitatively, to be independent of the details of the boundary conditions. This was also checked by doubling the domain size and the filter radius while keeping the resolutions fixed. Thus the phenomena reported below appear local, limited to the region where the confined topography is centered. Also, questions of sensitivity to computational resolution were tested by running all simulations both at resolutions 64×64 and 128×128 , with additional key tests at resolution 256×256 .

Finally, we must specify the values of the viscous coefficients in the evolution equation (14). When considering stationary flow, the inviscid solution is somewhat uninteresting from the point of view of form drag because, in a manifestation of D'Alembert's paradox, there turns out to be no drag at all in that case, as has been pointed out in Bannon (1980) and elsewhere. In other words, if the perturbation flow is stationary and confined (so that there is no possibility of transferring energy into the flow or to infinity), then there can be no energy input for there is no energy sink (see Batchelor, 1967). Thus we have to decide on what non-zero values to give for the viscous coefficients r and ν . To limit our search of parameter space, we have decided to set $\nu = 0.01$ and $r = 0.2$, taking these values from the parameter range explored by Verron and Le Provost (1985). In test cases we have varied these values by over an order of magnitude in each direction in order to verify that the phenomena reported are not qualitatively sensitive to these values; however, the results presented here, from sequences of simulations in which other parameters are varied, all have kept these viscous coefficients fixed at the values specified above.

Structure of the vorticity field

We consider flow over the elliptical hill with the large-scale flow started impulsively. That is, the flow is initially set at $U = 1$ everywhere. The large-scale component of the flow is maintained at that value thereafter. Initially there is no perturbation field, and

since there is no vorticity associated with the large-scale flow, there is initially no vorticity anywhere in the flow. As zero vorticity fluid is advected onto the topography, it must develop negative relative vorticity to compensate for the positive topographic contribution to the conserved potential vorticity, $q = \zeta + h$. Similarly, fluid advected off the hill must develop positive vorticity. Thus the earliest stage of evolution involves the creation of negative vorticity on the upstream side of the hill and positive vorticity on the downstream side. The later stages of evolution and, in particular, the final stationary flow depend on the strength of the topography. Here we shall take two extreme cases, $h_0 = 1$ and $h_0 = 100$, to illustrate the results for 'weak' and 'strong' topography, where the magnitudes are suggested by the circularly symmetric topography case in Verron and Le Provost (1985).

Weak topography

We illustrate the early evolution of the vorticity field over the peak of the topography in the case $h_0 = 1$ for positive and negative angles of attack in Figure 3. In panels (a) and (c), the very earliest stage is shown. The time is $t = 0.1$ after the beginning of the evolution. Here we have zoomed in on the flow over the topography, showing only the central area of size 3×3 of the full 5×5 computational domain. The fluid particles have so far been displaced approximately only a distance 0.1 in the downstream direction. This results in a dipolar vorticity distribution over the topography with roughly elliptical structure for both components. As the large-scale advection continues to have its effect, the core of the trailing positive relative vortex is advected downstream to eventually leave the computational domain, and this leaves primarily a negative vortex over the topography. This is shown in panels (b) and (d) at time $t = 1.4$. By this time there has been advection through distances greater than the topographic axes lengths a and b . The peak amplitude of the fixed relative vortex at that time is -0.84 , which is also the final stationary flow value. Thus unlike the inviscid case, the fixed vortex does not match the amplitude of the hill, and so the potential vorticity over the hill will not vanish. In this case, the relative vorticity is also not perfectly elliptical. Instead, it is relatively larger in magnitude on the upstream side than on the downstream side. We can understand this as simply the result of the fact that once the vorticity is created on any fluid particle being advected over the topography, the viscosity continually decreases the magnitude

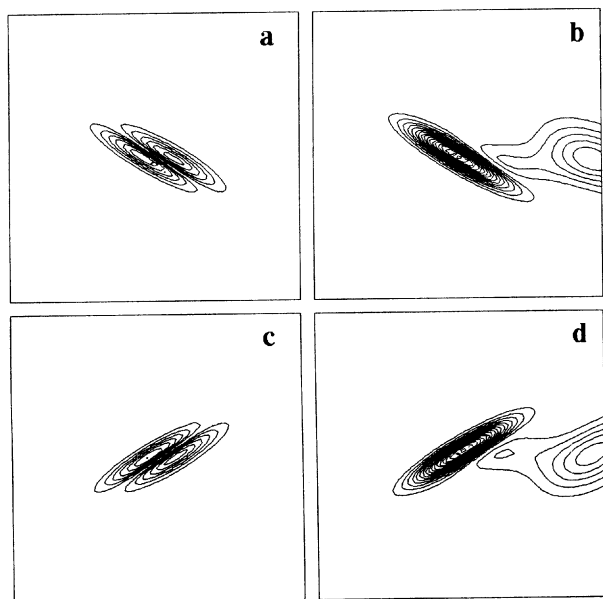


Figure 3. Vorticity contour plots showing the early evolution in the weak topography case, $h_0 = 1$. The large-scale flow comes from the left, and the top/bottom panels represent the vorticity for the case where the angle of attack is $\alpha = \pm 30^\circ$. The left panels correspond to time $t = 0.1$, while the right are taken at $t = 1.4$. The thick/thin curves correspond to positive/negative vorticity levels. The contour interval is 0.05. The zero vorticity level is not drawn. Only the central region of size 3×3 , of the computational domain of 5×5 , is shown.

of that vorticity as the particle moves downstream; hence, the vorticity will be stronger on the upstream side. This asymmetry to the negative relative vortex means that the potential vorticity field, $q = \zeta + h$ (not shown), over the topography will be dipolar with negative potential vorticity on the upstream side and positive on the downstream side, and this is also the case in the final stationary flow.

In the long term, the core of the positive relative vortex is shed downstream, eventually to be completely dissipated by viscous effects. However, a remnant of this vortex is left with a peak situated downstream of the topographic peak. The final stationary vorticity fields for cases representing four angles of attack are shown in Figure 4. The angles represented are $\alpha = -90^\circ, -30^\circ, 0^\circ$ and $+30^\circ$. These results are representative of the full set that we studied spanning the range $\alpha = \pm 90^\circ$ in 5° increments. For all of these cases, the local or perturbation flow due to the presence of the topography is weak in the sense that the lines of flow or the contours of total streamfunction

(not shown) are all nearly parallel to the large-scale flow direction.

For all angles of attack, there is a peak of positive relative vorticity downstream of the negative vorticity peak. It appears from these plots that the amplitude of both the positive and negative vorticity peaks depends strongly on the angle of attack. A quantitative measure of this dependence for the whole range of attack angles is shown in Figure 5a. We graph the extremal values of relative vorticity as a function of α . The dashed curve corresponds to the absolute value of the negative vorticity peak value, while the solid curve is the value of the positive vorticity peak value. The negative vorticity is strongest at $\alpha = 90^\circ$ (coming up to 95% of the value of the topography maximum) and weakest for $\alpha = 0^\circ$ and *vice versa* for the positive vorticity. To help understand these results, consider the fluid element which comes from upstream, crosses the peak of the topography, and then moves downstream. A fluid element approaching from up-

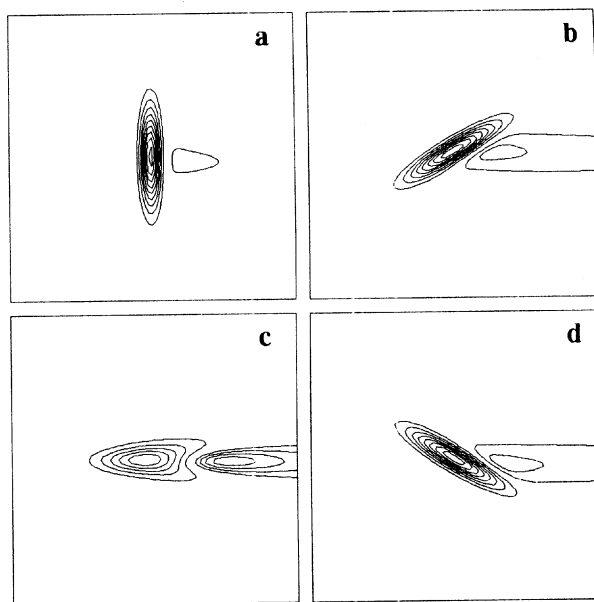


Figure 4. Contour plots of the stationary relative vorticity field for the weak topography case, $h_0 = 1$, for various angles of attack. These panels represent the stationary vorticity field for flow over the elliptical topography for the angles of attack $\alpha = -90^\circ, -30^\circ, 0^\circ$ and $+30^\circ$, ordered from left to right, top to bottom. The thick curves correspond to positive vorticity levels spaced 0.05 units apart, while the thin curves correspond to negative vorticity levels spaced 0.1 units apart. The zero vorticity level is not drawn. Only the central region of size 3×3 , of the full computational domain of 5×5 , is shown.

stream has zero relative vorticity, and, for each 'step' that it takes going uphill, it acquires exactly enough negative vorticity to balance the positive topographic contribution in the conservation of the potential vorticity. Thus for inviscid flow the stationary potential vorticity is exactly zero everywhere with relative vorticity being exactly anticorrelated with the topography, $\zeta = -h$. With viscosity, however, the relative vorticity generated on the fluid element by the topographic effect also dissipates continuously. Thus, when this fluid element reaches its highest point on the topography, its relative vorticity will be weaker in strength than it would have been inviscidly. Then, as it descends the hill, the positive vorticity generated by the conservation of potential vorticity more than cancels the relative vorticity remaining from its climb with the destructive effects of viscosity acting. Thus, net positive relative vorticity will result on the descent. Of course, the positive relative vorticity on the fluid element will continue to diminish as it moves downstream. Furthermore, we see that the strength of the positive vortex depends strongly on the angle of attack. Of all the cases shown in Figure 4, the ascent to the top of the hill by the fluid element is shortest for $\alpha = 90^\circ$. In that case, there is little time for viscosity to act during the ascent and descent. Hence, the discrepancy between the total vorticity production during those two phases is relatively small. In contrast, in the case with $\alpha = 0^\circ$, the excursion to the top is the longest, and hence the effect of viscous decay on the vorticity is the greatest. Thus the positive relative vortex generated on the descent will be the strongest of any angle of attack.

As we shall see in section 4, it is also of interest to consider the position of the positive relative vortex in relation to the topography. Clearly from Figure 4, the peak of positive vorticity will lie nearly on the x -axis. A secondary advective effect, due to the non-zero strength of the negative vortex, displaces the peak of positive vorticity to a position below the x -axis. The negative vortex over the hill induces positive velocity in the y direction (i.e., $v = \partial\psi/\partial x > 0$) on the upstream side of the topography and negative v on the downstream side. This secondary flow tends to displace the positive vorticity in an arc in the clockwise direction about the center of the topography. In Figure 5b we plot the angle for the position of the peak of the positive vorticity measured from the direction of the nose of the topography. Also on the same graph is a dashed curve showing the line of no displacement. The fact that the observed displace-

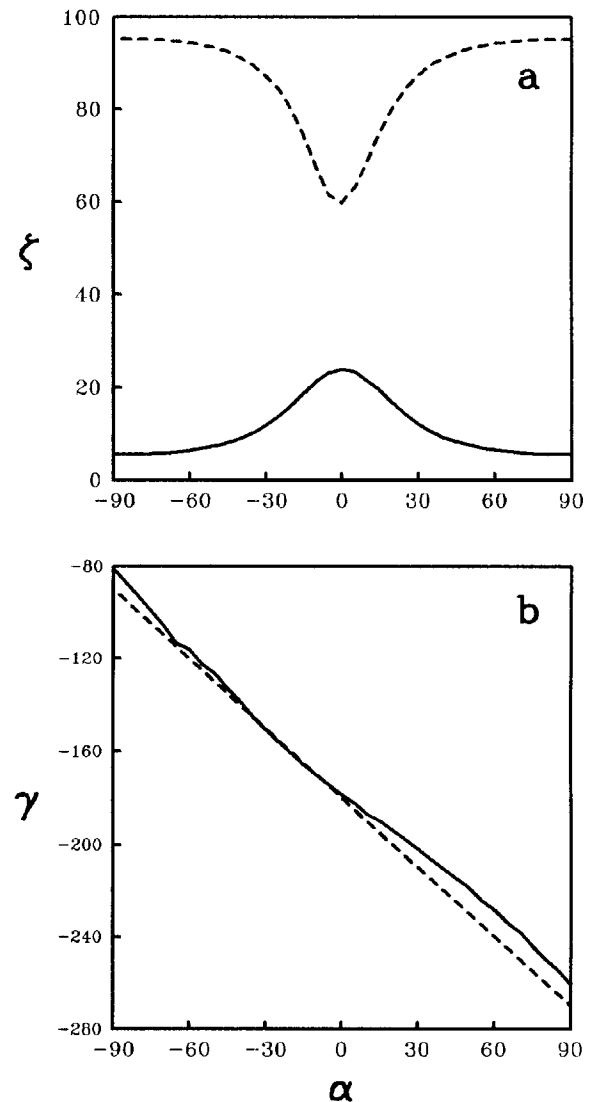


Figure 5. Position and amplitude of relative vorticity extrema in the weak topography case, $h_0 = 1$. (a) The solid curve shows the angular position of the peak of positive relative vorticity. This angle is measured from the direction of attack, that is, from the direction along the long topographic axis facing in the upstream direction. The dashed curve shows the angular position, measured in the same way, of a point on the x -axis (i.e. the curve of no displacement). (b) The solid/dashed curve shows the magnitude of the vorticity at the extremal positive/negative value.

ment angles lie on a line that is predominantly above the dashed line is due to the clockwise displacement of the positive vortex.

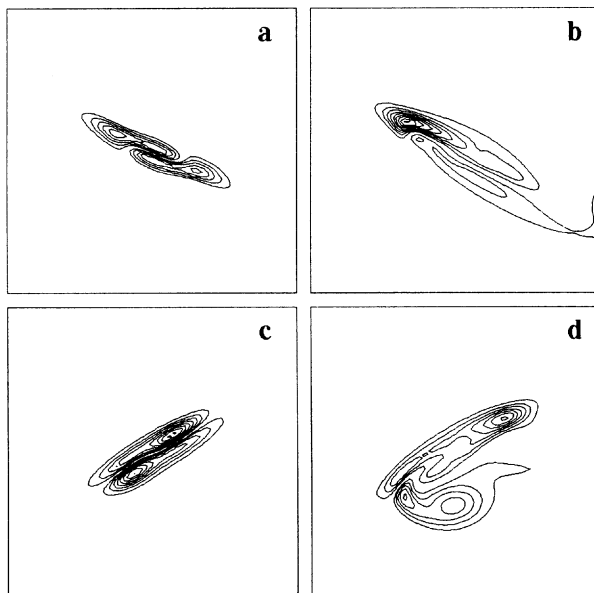


Figure 6. Contour plots showing the early evolution for the relative vorticity field in the strong topography case, $h_0 = 100$. The large-scale flow comes from the left, and the top/bottom panels represent the vorticity for the case where the angle of attack is $\alpha = \pm 30^\circ$. The left panels correspond to time $t = 0.1$, while the right are taken at $t = 1.4$. The thick/thin curves correspond to positive/negative vorticity levels. The contour interval is 4 in panels (a) and (c) and 2 in panels (b) and (d). The zero vorticity level is not drawn. Only the central region of size 3×3 , of the full computational domain of 5×5 , is shown.

Strong topography

The structure of the vorticity field in the strong topography case contrasts greatly with that in the weak case. At the earliest times, when the large-scale flow is first applied, the structure of the generated vorticity field must be the same as in the weak topography case since the same arguments for its generation apply again. However, that early phase is very short lived because, for sufficiently strong topography, the vorticity generated over the topography can induce flows comparable in speed to the large-scale flow. In Figure 6, we show the early evolution for the example corresponding to $h_0 = 100$, at the same times as shown in figure (3) for the weak topography case. Already at time $t = 0.1$, when the fluid has only been advected a short distance, the induced vortices are strong enough to make their mutual interaction as important as the advection by the large-scale flow. By this time, the early simple structure like that shown

in Figure (4), has already been disrupted by the dynamics of the induced vortices. Intuitive arguments are much more difficult in the strong topography case, and less trustworthy, so perhaps it is best just to attempt a description at this point. In the $\alpha = +30^\circ$ case shown in Figure 6, panels (a) and (b), we see that local vortex dynamics has already strongly distorted the symmetric dipolar field. The positive and negative vortices have both developed two centers. Later these interact in a complicated way and the positive vorticity temporarily breaks into several pieces. The strongest positive vorticity center is eventually shed downstream and is just barely visible at the edge of the region shown in panel (b), and the rest of the positive vorticity joins together to form an elongated patch. Also in panel (b) we note that the negative vorticity has become concentrated at the 'forward end' or 'nose' of the topography, while the residual part of the negative vortex has become elongated along the upstream side of the topography. In the $\alpha = -30^\circ$ case shown in Figure 6 panels (c) and (d), the $t = 0.1$ vorticity structure has not departed as severely from

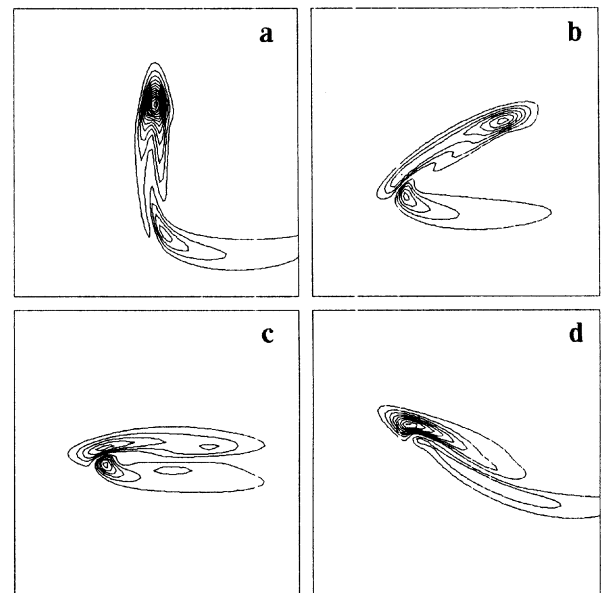


Figure 7. Contour plots of the relative vorticity field for the strong topography case, $h_0 = 100$. These panels represent the stationary vorticity field for flow over the elliptical topography for the angles of attack $\alpha = -90^\circ, -30^\circ, 0^\circ$ and $+30^\circ$, ordered from left to right, top to bottom. The thick/thin curves correspond to positive/negative vorticity levels spaced 2.0 units apart. The zero vorticity level is not drawn. Only the central region of size 3×3 , of the full computational domain of 5×5 , is shown.

the weak topography case. However, note the tendency for the negative vortex to peak over the 'tail' or downstream end of the topography, while the positive vortex concentrates at the 'nose.' Later, the positive vortex forms a secondary peak of weaker amplitude as seen in panel (d), but this is then shed downstream.

The final stationary configurations for these two attack angles are shown in Figure 7, along with the $\alpha = 0^\circ$ and $\alpha = 90^\circ$ cases. The negative vortex is no longer elliptical. For all the attack angles, the negative vortex is more concentrated at one end of the topography, and the positive vortex is now no longer simply trailing on the x-axis. Even though the negative vortex is now, at its most intense point, only 30% of the peak amplitude of the topography, the topography is so strong that the nonlinear term $J(\psi, \zeta)$ competes with the large-scale advection. The negative vortex here is intense enough to strongly displace the trailing positive vortex from the positive x-axis. For $-90^\circ \leq \alpha < -15^\circ$, the negative vortex is concentrated at the tail of the topography, while the positive vortex is concentrated at the nose, although it also has a broad tail elongated in the downstream direction. As α increases, a secondary negative vorticity peak develops. This is just beginning in panel (b) at $\alpha = -30^\circ$. From $-30^\circ \leq \alpha < 0^\circ$, the negative vorticity has two peaks, the one near the tail, induced primarily by the large-scale advection of fluid, and the second induced by the influence of the positive vortex advecting fluid off the peak and upstream along the crest of the hill. At $\alpha = -15^\circ$, the negative vorticity peak near the nose dominates, comprising, with the primary positive vortex, a dipole at the nose. At $\alpha = 0^\circ$ (panel c), we see a secondary positive vortex has also developed, and by $\alpha = +30^\circ$ that trailing positive vortex peak has higher amplitude than the one at the nose. For moderate positive angles α , the two distributions are broad forming a dipole with positive vorticity on the leading edge of the topography and negative vorticity concentrated on the nose and along the crest. The transitions from the dominance of the original vortices present at $\alpha = -90^\circ$ to the secondary vortices that develop are shown by the graph in Figure 8b. The angle is measured from the direction of the nose, so the transition from 180° to 0° , on the dashed curve, corresponds to the transition from the trailing negative vortex at the tail to the leading vortex induced by the positive vortex. The transition from 0° to -180° , on the solid curve, corresponds to the transition from the leading positive vortex at the nose to the trailing positive vortex.

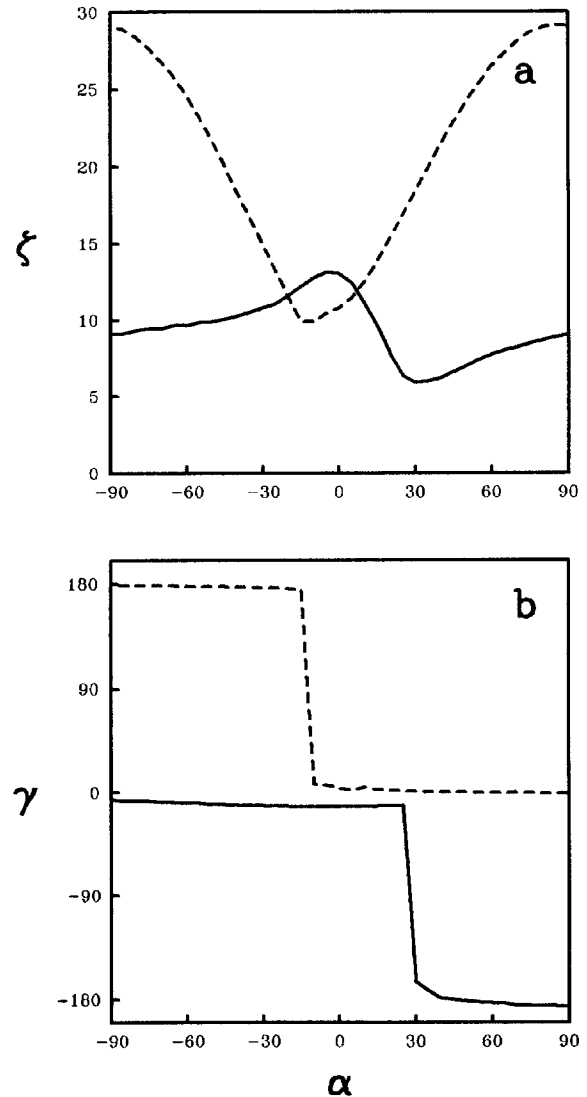


Figure 8. Position and amplitude of relative vorticity extrema in the strong topography case, $h_0 = 100$. (a) The solid/dashed curve shows the angular position of the peak of positive/negative relative vorticity. This angle is measured from the direction of attack, that is, from the direction along the long topographic axis facing in the upstream direction. (b) The solid/dashed curve shows the amplitude of vorticity at the extremal positive/negative value.

In Figure 8a, we show the magnitude of the vorticity extrema for the full range of attack angles. The dependence on attack angle is somewhat more complicated than in the weak topography case (note especially the minimum in the amplitude of the peak positive vorticity at $\alpha = 30^\circ$). Nevertheless, like the

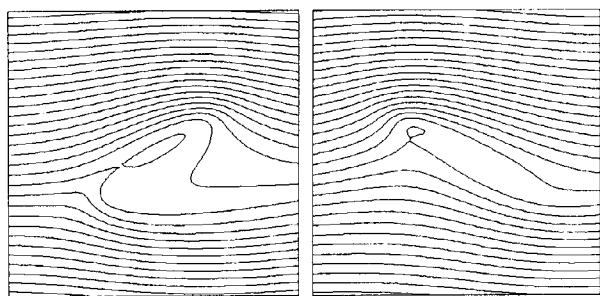


Figure 9. Contour plot of the stationary total streamfunction for the strong topography case, $h_0 = 100$. In panel (a), $\alpha = -30^\circ$, and in panel (b) $\alpha = +30^\circ$. The contour interval is 0.1. Only the central region of size 3×3 , of the full computational domain of 5×5 , is shown.

weak topography case, the negative vortex is weakest/strongest for small/large angle of attack, and the positive vortex is strongest for small angle of attack. Note that the maximum negative vorticity extremum is only 30% of the peak topographic amplitude as opposed to the 95% that is reached in the weak topography case. Also, looking at the vorticity contour plots, we see that the strong topography case is far from the inviscid solution, $\zeta = -h$.

In Figure 9, we show the total streamfunction for the flow. Here we see that the induced negative vortex is strong enough to reverse the flow locally and produce closed contours. We should mention that such closed contours, or recirculating regions, would not be possible for the stationary flow if the only dissipation acting was Ekman bottom drag. This follows from the fact that on any closed contour the fluid element circulating over and over again on the same path would have no way to replenish its decaying vorticity; however, the presence of Laplacian friction allows these closed contours because there is then diffusion of vorticity across them. As for the border between values of topography for which these closed contours do or do not form, this will depend on the attack angle as well as the strength of the topography.

Remarks on the position of the cyclone in the stationary flow

The discussion above strongly suggests that in the stationary flow there is always a cyclone to be found near the hill, even if this is just a remnant of the original transient cyclone. This is fairly straightforward to prove in the case in which the bottom drag parameter, r , is non-vanishing. The equation for the steady

state is, from (14),

$$J(\psi - Uy, \zeta + h) = -r\zeta + \nu \nabla^2 \zeta. \quad (15)$$

If we assume that the that ζ and h vanish sufficiently rapidly as the distance from the center of the hill increases, then on integrating over the whole plane, we obtain

$$r \int \int \zeta dx dy = 0. \quad (16)$$

Thus the circulation must vanish. Since ζ vanishes at infinity, this means that there must be both positive and negative extrema somewhere on the plane. Unfortunately, this proof tells us nothing about the case in which $r = 0$. Our experience with a few test cases shows that even in that situation there is still a remnant cyclone in the stationary flow as long as ν is nonvanishing.

At an extremum of ζ , its gradient vanishes. Hence, from (15), we have

$$J(\psi - Uy, h)_\pm = -r\zeta_\pm + (\nu \nabla^2 \zeta)_\pm. \quad (17)$$

where all the terms are evaluated at the position, \mathbf{r}_+ of the maximum or at \mathbf{r}_- , the position of the minimum. At the maximum, we have $\zeta = \zeta_+ > 0$ and $(\nabla^2 \zeta)_+ < 0$, and thus $J(\psi - Uy, h)_+ < 0$. This implies that the position of the peak must lie on the topography. Similarly, one can show that the minimum ζ must also lie over the topography. Now with the Gaussian hill, the topography technically covers the plane, but for compact topography, the extrema of vorticity would clearly be restricted to lie in the compact region defined by the hill. In the case of strong flow, in which U dominates ψ , we further have that

$$U \left. \frac{\partial h}{\partial x} \right|_+ < 0 \quad (18)$$

implying that the cyclone must in that case (weak topography) be on the downstream side of the hill.

Form drag in the stationary flow

Topographic form drag is the net force exerted on the flow by the topography along the direction of the large-scale flow. Consequently, the drag is the negative of the net force acting on the topography in flow direction. To calculate the total force, \mathcal{F} , acting on the topography, we integrate the pressure force over the entire surface of the topography: $\mathcal{F} = - \int \int \mathbf{p} \mathbf{n} da$, where \mathbf{n} is the outward unit normal vector from the surface of the topography, and da is the element of

area on the surface. Since the surface of the topography is defined by $z = -H_0 + \Delta H(x, y)$, we have the standard results:

$$\mathbf{n} = \frac{(-\partial\Delta H/\partial x, -\partial\Delta H/\partial y, 1)}{\sqrt{1 + (\partial\Delta H/\partial x)^2 + (\partial\Delta H/\partial y)^2}}, \quad (19)$$

and

$$da = \sqrt{1 + (\partial\Delta H/\partial x)^2 + (\partial\Delta H/\partial y)^2} dx dy. \quad (20)$$

Thus, the total force, \mathcal{F} , in the x -direction is

$$\mathcal{F} \cdot \hat{\mathbf{x}} = \int \int p \frac{\partial\Delta H}{\partial x} dx dy = f\rho \int \int \Psi \frac{\partial\Delta H}{\partial x} dx dy, \quad (21)$$

where we have introduced the definition of the streamfunction in terms of the pressure in the last line. Consider, for example, the case of flow in the positive x direction impinging on a hill. If the pressure is higher on the upstream side of the topography, where $\partial\Delta H/\partial x$ is positive, than on the downstream side, where $\partial\Delta H/\partial x$ is negative, then there is a net force on the topography in the direction of the flow, as we would expect. If we integrate by parts, we can express these results in terms of the pressure gradient or, equivalently, the velocity field. Using the definition of the scaled topography, and integrating by parts, we obtain

$$\mathcal{F} \cdot \hat{\mathbf{x}} = -\rho H_0 \int \int h \frac{\partial\psi}{\partial x} dx dy. \quad (22)$$

Thus we see that an enhanced pressure gradient on one side of the topography relative to the other, yields a net force on the topography.

The drag on the flow is the negative of the force on the topography. The product ρH_0 is just the mean mass per unit area, and it is convenient to factor this out of the definition for drag. Thus we shall define this normalized drag as

$$D = \int \int h \frac{\partial\psi}{\partial x} dx dy \quad (23)$$

(cf. Bannon 1985, Carnevale and Frederiksen 1987).

Considering the drag in the case of stationary flow, we first check that the drag in the inviscid case is zero as discussed above. The solution to the inviscid problem is given by $q = 0$, that is, $\nabla^2\psi = -h$. Substitute $-\nabla^2\psi$ for h directly in the expression for D and integrate by parts. All that remains after the integration is a boundary term at infinity that vanishes. Next, we turn to numerical results for the stationary states

with viscosity. As in the case where we considered the structure of the vorticity field, we will see that the behavior of the drag is rather different in the weak and strong topography limits.

Weak topography

To obtain the stationary flows for given topography and large-scale flow velocity, we simulated the evolution, from an initial condition of uniform flow, long enough in time for all transients to die down. In Figure 10, we show the results from a series of such simulations performed with the periodic boundary condition code with spatial filter. In this series, the angle of attack of the topography was varied from -90° to $+90^\circ$ in 5° increments. As in the previous section, the weak topography case is represented by using the topographic amplitude $h_0 = 1$. Since the form drag is always negative, opposing the large-scale flow, we consider only its magnitude. In Figure 10a, we plot the form drag in the stationary state as a function of the attack angle. The form drag is greatest when the long axis of the topography is perpendicular (i.e., $\alpha = \pm 90^\circ$) rather than parallel ($\alpha = 0^\circ$) to the flow. As we might have expected from the discussion in the previous section on the vorticity structure, the curve is not symmetric about $\alpha = 0^\circ$. It appears that the form drag is stronger for a positive angle of attack than for a negative angle of the same magnitude. In Figure 10b, we plot the relative variation of that difference, that is, we plot $(|D(\alpha)| - |D(-\alpha)|)/|D(\alpha)|$, where $D(\alpha)$ is the form drag for a given angle of attack. The Figure shows that the difference is greatest when the size of the attack angle is about 20° , with a 2% variation at that angle. For somewhat higher topographies ($h_0 \approx 20$), the relative variation reaches about 20%, as we shall see below.

For the weak topography case, form drag dependence on attack angle can be predicted from perturbation theory. To examine the effects of weak topography, we begin by rewriting the stationary form of equation (14) as

$$U \frac{\partial\zeta}{\partial x} + r\zeta - \nu \nabla^2\zeta = -U \frac{\partial h}{\partial x} - J(\psi, \zeta + h). \quad (24)$$

We assume the primary balance for weak topography is between the terms on the left, which are linear in the vorticity, and the first forcing term on the right, $-U\partial h/\partial x$. This permits us to treat the quadratically nonlinear Jacobian term as a small perturbation. It also means that at lowest order the streamfunction is linear in the topography, and all succeeding terms are

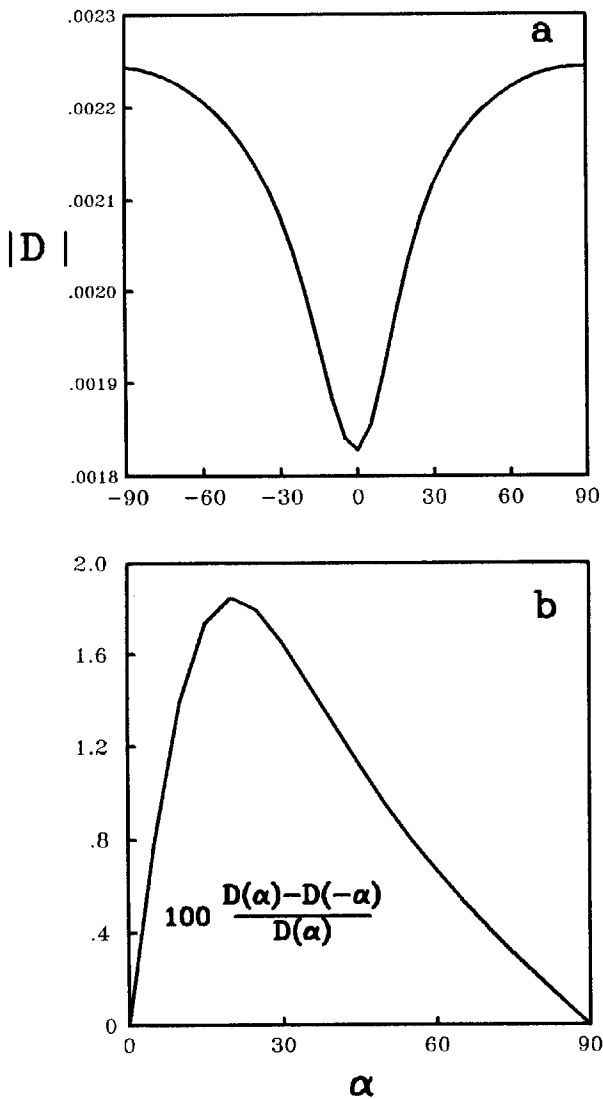


Figure 10. Form drag for the weak topography case, $h_0 = 1$. This data is taken from simulations using the spatially cutoff code. (a) The absolute value of the stationary form drag is plotted as a function of attack angle. (b) The percent of relative variation of the difference between the drag at positive and negative angles of attack is plotted versus attack angle. Specifically, the graph represents $100(D(\alpha) - D(-\alpha))/D(\alpha)$, where $D(\alpha)$ is the form drag for a given angle of attack, α .

of higher integral order. Thus we write

$$\psi = \psi^{(1)} + \psi^{(2)} + \psi^{(3)} + \dots, \quad (25)$$

$$\zeta = \zeta^{(1)} + \zeta^{(2)} + \zeta^{(3)} + \dots, \quad (26)$$

where $\zeta^{(n)} = \nabla^2 \psi^{(n)} = O(h_0^n)$.

To evaluate the terms in the perturbation series, we first take the continuous Fourier transform in both x and y to obtain

$$g_{\mathbf{k}}^{-1} \zeta_{\mathbf{k}} = -ik_x U h_{\mathbf{k}} - J_{\mathbf{k}}(\psi, \zeta + h). \quad (27)$$

Here the linear Green function $g_{\mathbf{k}}$ is given by

$$g_{\mathbf{k}} = \frac{1}{ik_x U + d_k}, \quad (28)$$

where $d_k = r + \nu k^2$, and $J_{\mathbf{k}}(A, B)$ is the Fourier transform of the Jacobian of fields A and B . An explicit formula for $J_{\mathbf{k}}(A, B)$ in terms of the Fourier transforms of A and B is given in the appendix.

The first and second order solutions can then be written as

$$\zeta_{\mathbf{k}}^{(1)} = -ik_x U g_{\mathbf{k}} h_{\mathbf{k}}, \quad (29)$$

and

$$\zeta_{\mathbf{k}}^{(2)} = -g_{\mathbf{k}} J_{\mathbf{k}}(\psi^{(1)}, \zeta^{(1)} + h). \quad (30)$$

The form drag can now be calculated order by order. Directly from the formula (23) for the form drag and the fact that the streamfunction at lowest order is linear in the topography, we see that the form drag is quadratic in the topography at lowest order. Thus the perturbation series for the form drag will be

$$D = D^{(2)} + D^{(3)} + D^{(4)} + \dots \quad (31)$$

Using the Fourier transform within the formula for the form drag, we have

$$D = \int \int h \frac{\partial \psi}{\partial x} dx dy = - \int \int \frac{ik_x}{k^2} \zeta_{\mathbf{k}} h_{-\mathbf{k}} \frac{d^2 k}{(2\pi)^2}. \quad (32)$$

Then by direct substitution of (29) into (32), we obtain

$$D^{(2)} = -U \int \int \frac{k_x^2}{k^2} g_{\mathbf{k}} |h_{\mathbf{k}}|^2 \frac{d^2 k}{(2\pi)^2} \quad (33)$$

$$= -U \int \int \frac{k_x^2 (-ik_x U + d_k) |h_{\mathbf{k}}|^2}{k^2 (U^2 k_x^2 + d_k^2)} \frac{d^2 k}{(2\pi)^2} \quad (34)$$

Notice that the last expression is decomposed into a real and imaginary part. But the form drag is a real quantity. The vanishing of the imaginary part of the integral can be checked by considering the change of sign $\mathbf{k} \rightarrow -\mathbf{k}$ for the dummy integration variables. Since the topography is real we have the Hermiticity constraint, $h_{\mathbf{k}}^* = h_{-\mathbf{k}}$, and so $|h_{\mathbf{k}}|^2$ is unaltered by this sign change. Thus we see that the imaginary part of the integrand changes sign under this sign reversal

and so must vanish on integration over the range from $-\infty$ to $+\infty$ for k_x and k_y . Finally we have

$$D^{(2)} = -U \iint \frac{k_x^2 d_k |h_{\mathbf{k}}|^2}{k^2 (U^2 k_x^2 + d_k^2)} \frac{d^2 k}{(2\pi)^2}. \quad (35)$$

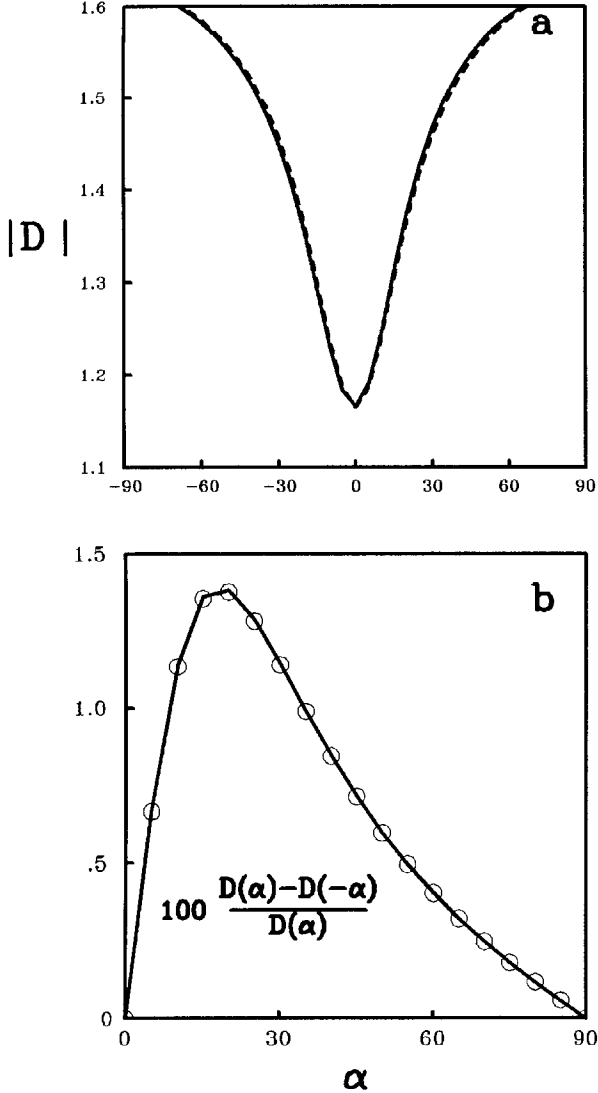


Figure 11. Form drag from weak topography perturbation theory for $h_0 = 1$. (a) The solid curve is the form drag from the fully nonlinear simulation. The dashed curve is the prediction of the lowest order perturbation theory, $D^{(2)}$ (here in units of 10^{-3}). (b) The open circles mark the results for the relative variation of the difference between the drag at positive and negative angles of attack for the fully nonlinear simulations. The solid curve shows the prediction of the perturbation theory truncated at next to lowest order, that is with $D \approx D^{(2)} + D^{(3)}$.

It is difficult to apply this perturbation theory, meant for the infinite domain, directly to the simulations with the channel and radiation boundary conditions or the spatially filtered simulation. However, for simulations with periodic boundary conditions, the result is simply a discretization of the continuous formulas. We used a quasi-geostrophic doubly periodic code to calculate the stationary solutions for the same set of experiments used to make Figure 10. In Figure 11a, we compare the actual result for the dependence on α for the full nonlinear doubly periodic calculation with the lowest order result. Although the quantitative values are somewhat different than for the case with the spatial filter, qualitatively they are alike. In Figure 11a, we see that the lowest order perturbation theory does account for most of the form drag. The small difference is essentially due to the next order term in the theory, but before proceeding to show that, let us first note that the lowest order form drag, $D^{(2)}$ is symmetric in the attack angle. In fact, this will be the case for any topography with a reflection symmetry. Let us include the dependence on the attack angle explicitly. We can define the attack angle either with reference to the angle between the line of symmetry or perpendicular to it. Then we can write $h(x, y; \alpha) = \phi(x', y')$, where x' and y' are just the rotated coordinates defined previously in equations (11) and (12). A reflection symmetry corresponds to the fact that either $\phi(x, y) = \phi(-x, y)$ or $\phi(x, y) = \phi(x, -y)$. We shall write the Fourier transform of $h(x, y; \alpha)$ as $\hat{h}_{\mathbf{k}}(\alpha)$. By using the fact that rotations do not change area, this Fourier transform is found to be

$$h_{\mathbf{k}}(\alpha) = \hat{\phi}(k'_x, k'_y), \quad (36)$$

where $\hat{\phi}(k_x, k_y)$ is the Fourier transform of $\phi(x, y)$, and

$$k'_x = k_x \cos \alpha + k_y \sin \alpha, \quad (37)$$

$$k'_y = -k_x \sin \alpha + k_y \cos \alpha. \quad (38)$$

By direct substitution in equation (35), we have

$$D^{(2)}(\alpha) = -U \iint \frac{k_x^2 d_k |\hat{\phi}(k'_x, k'_y)|^2}{k^2 (U^2 k_x^2 + d_k^2)} \frac{d^2 k}{(2\pi)^2} \quad (39)$$

$$= -U \iint \frac{k_x^2 d_k}{k^2 (U^2 k_x^2 + d_k^2)} \quad (40)$$

$$\times |\hat{\phi}(k_x \cos \alpha + k_y \sin \alpha, -k_x \sin \alpha + k_y \cos \alpha)|^2 \frac{d^2 k}{(2\pi)^2}. \quad (41)$$

Thus,

$$D^{(2)}(-\alpha) = -U \iint \frac{k_x^2 d\mathbf{k}}{k^2(U^2 k_x^2 + d_k^2)} \quad (42)$$

$$\times |\hat{\phi}(k_x \cos \alpha - k_y \sin \alpha, k_x \sin \alpha + k_y \cos \alpha)|^2 \frac{d^2 k}{(2\pi)^2}. \quad (43)$$

If $\phi(x, y) = \phi(-x, y)$, which implies $\hat{\phi}(-k_x, k_y) = \hat{\phi}(k_x, k_y)$, then the substitution $k_x \rightarrow -k_x$ shows that $D^{(2)}(-\alpha) = D^{(2)}(\alpha)$. If $\phi(x, y) = \phi(x, -y)$, then the same point is demonstrated by the change of variables $k_y \rightarrow -k_y$.

These results show that the asymmetry in the form drag, as seen in Figure 10, must come from higher order terms in the perturbation theory. We shall next demonstrate that for $h_0 = 1$ the second term in the perturbation series captures the observed deviation from symmetry very well. That term, $D^{(3)}$, is derived in general form in the appendix. If the topography has the point reflection symmetry $h(x, y) = h(-x, -y)$, as is the case for the elliptical topography, then the expression for $D^{(3)}$ simplifies and we have

$$D^{(3)} = -U^3 \int 2d_p d_q q^2 k_x^2 p_x q_x b_{\mathbf{k}} b_{\mathbf{p}} b_{\mathbf{q}} \mathcal{D}_{\mathbf{k}\mathbf{p}\mathbf{q}}, \quad (44)$$

where

$$b_{\mathbf{k}} \equiv \frac{h_{\mathbf{k}}}{k^2(U^2 k_x^2 + d_k^2)}, \quad (45)$$

and

$$\mathcal{D}_{\mathbf{k}\mathbf{p}\mathbf{q}} = \hat{\mathbf{z}} \cdot \mathbf{p} \times \mathbf{q} (2\pi)^2 \delta(\mathbf{k} + \mathbf{p} + \mathbf{q}) \frac{d^2 k}{(2\pi)^2} \frac{d^2 p}{(2\pi)^2} \frac{d^2 q}{(2\pi)^2}, \quad (46)$$

as shown in the appendix.

If, in addition to the symmetry of reflection in a point, the topography is also symmetric to reflection through a line, then we can show that $D^{(3)}(\alpha) = -D^{(3)}(-\alpha)$. For example, if the topography is symmetric about the y' -axis, then $h_{k_x, k_y}(\alpha) = \hat{\phi}(k'_x, k'_y) = \hat{\phi}(-k'_x, k'_y) = h_{-k_x, k_y}(-\alpha)$. Thus, a change of variables in which all k_x, p_x, q_x change sign in the expression for $D^{(3)}(-\alpha)$ shows that the integrand is simply the negative of that in the expression for $D^{(3)}(\alpha)$ (note that $\hat{\mathbf{z}} \cdot \mathbf{p} \times \mathbf{q}$ changes sign). Similarly if $h_{k_x, k_y}(\alpha) = h_{k_x, -k_y}(-\alpha)$, then a change of variables in which all k_y, p_y, q_y change sign, in the expression for $D^{(3)}(-\alpha)$, shows again that the integrand is simply the negative of that in the expression for $D^{(3)}(\alpha)$. By rotation, this result can be further extended to

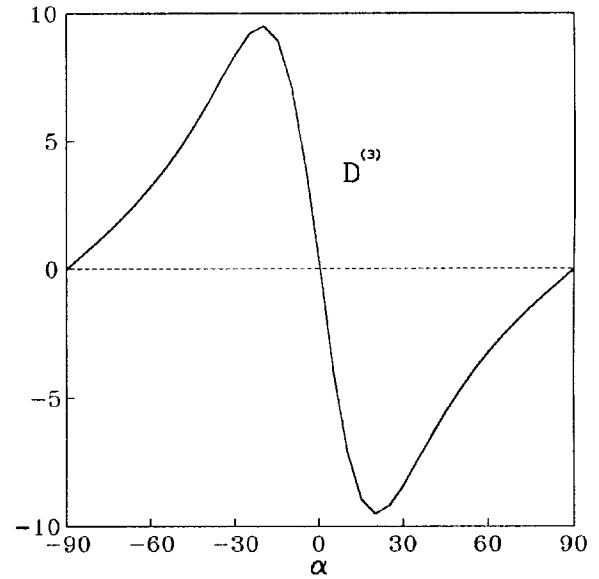


Figure 12. Antisymmetric contribution to the form drag from the next to lowest order in perturbation theory, $D^{(3)}(\alpha)$. The calculation is made for the doubly periodic boundary condition case. This contribution accounts almost entirely for the difference between the dashed and solid curve in Figure 11a. $D^{(3)}(\alpha)$ is measured here in units of 10^{-6} .

the case for topography with reflection symmetry in any horizontal line. For the periodic boundary condition case, it is again an easy matter to calculate the theoretical drag by discretizing the Fourier representation. In Figure 11b, we show the relative difference between the form drag for positive and negative angles of attack (open circles) calculated from the fully nonlinear simulations with periodic boundary condition. These values are compared to the predictions (solid curve) from the perturbation theory truncated at the $D^{(3)}(\alpha)$ contribution. For this weak topography case, the match is almost perfect. The form drag contribution coming solely from $D^{(3)}(\alpha)$ is shown in Figure 12, and is antisymmetric as anticipated.

Strong topography

As we increase the amplitude, h_0 , of the topography, the perturbation theory can be expected to fail. In two series of experiments, in which the angle of attack was fixed at $\pm 30^\circ$ respectively, the topography amplitude was varied from 1 to 150. The absolute values of the stationary form drag for these experiments are plotted in Figure 13a. The solid/dashed curve corresponds to the experiments with attack angle

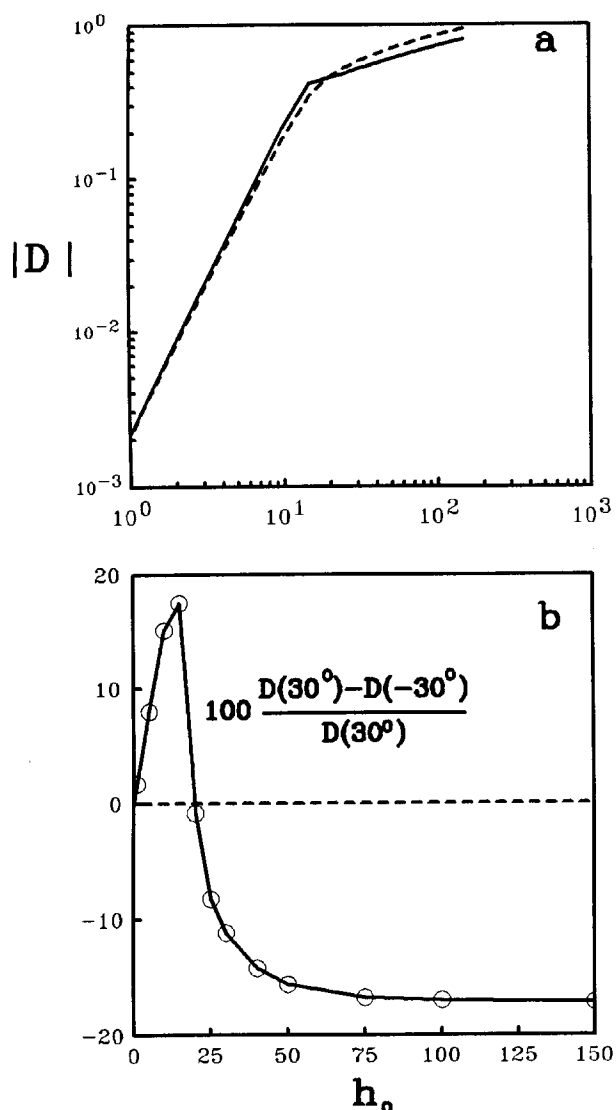


Figure 13. Form drag as a function of topographic height. (a) Two series of experiments are represented, with the angle of attack, α , fixed in each series at $+30^\circ$ and -30° respectively. The solid/dashed curve shows the absolute value of the stationary form drag from the experiments with $\alpha = +/\!-30^\circ$. Note that at $h \approx 15$ there is a cross-over between the regime in which the positive angle of attack gives a stronger form drag to the regime with just the reverse relationship. b) The relative difference in form drag strength between the plus and minus 30° cases is plotted as a function of topographic strength (the dashed line is simply the zero level).

$+/\!-30^\circ$. Firstly, we note that for the range of topography roughly from $h_0 = 1$ to $h_0 = 15$, the form drag for both curves is approximately a quadratic function

of h_0 . This is what one would expect in a weak topography regime where $D^{(2)}$, the lowest order approximation to the form drag, would dominate. Also note that, in this region, the strength of the form drag for the positive angle is stronger than that for the negative angle. Near $h_0 = 15$ there is a transition to a new regime where the scaling with topography no longer follows the quadratic law. In the strong topography regime, the drag seems to increase with topography amplitude roughly as $h_0^{0.3}$. Also in the strong topography regime, the relation between the form drag for positive and negative angles has reversed, with negative angles of attack corresponding to stronger form drag than positive angles. This last point is emphasized in Figure 13b, where the relative difference in form drag strength between the plus and minus 30° cases is plotted as a function of topographic strength.

As an example of the functional dependence of the form drag on angle for a case of strong topography, we plot this relation for the case of $h_0 = 100$ in Figure 14a (solid curve). There have been several papers which discuss in part the theory of strong topographic forcing (cf., Pierrehumbert and Malguzzi, 1984); nevertheless, we have not been able to predict the shape of this form drag curve. We note that this curve is somewhat broader about $\alpha = 0^\circ$ than the corresponding curve for $h_0 = 1$ in Figure 10a. As an aid to judging the symmetry and smoothness of the curve, we have also plotted the symmetric dashed curve corresponding to $A \sin^2 \alpha + B \cos^2 \alpha$, where A and B were chosen so that the two curves would have the same extremal values. In Figure 14b, we plot the relative difference in strengths between positive and negative angles of attack. The shape of the curve is similar to that shown in Figure 10b except, of course, for the sign since in this regime the negative angles correspond to stronger form drag. Here we see that the maximum difference is about -18% at around attack angle $|\alpha| = 20^\circ$. This is a great deal stronger than the $h_0 = 1$ case, but similar to the results for $h_0 = 15$ (see Figure 13b), which is still in the regime where the positive attack angle leads to the stronger form drag.

The crossover from the weak to the strong topography regime seems, from Figures 13a and 13b, to occur roughly near $h_0 = 15$. As we noted above, in section 3, when $h_0 = 1$ the total streamfunction is only slightly perturbed from that for uniform flow, but for topographies as strong as $h_0 = 100$, a Taylor column, i.e. a region of recirculating, closed streamlines is evident (cf. Figure 9). It is tempting to try

to attribute the transition of the form drag behavior in the weak and strong limits with the occurrence of the Taylor column. However, the formation of Taylor columns occurs in these simulations for topographic amplitudes above roughly $h_0 = 50$, depending somewhat on the angle of attack, and not at $h_0 = 15$. Of course, in the regime from $h_0 = 15$ to $h_0 = 50$, the streamlines are strongly distorted from the unperturbed case of uniform flow even though closed contours do not form. The behavior of the form drag as a function topographic height, as well as its dependence on attack angle, are better understood in terms of the structure of the stationary vorticity field, as we will now consider further.

Effects of the structure of the vorticity field

In order to try to build some intuitive understanding of these results on the form drag, we shall examine the vorticity field associated with the stationary flow for the weak and strong topography cases. Consider the $\alpha = -90^\circ$ case in Figure 4a along with the formula (23) for the form drag. The negative vortex over the hill induces a positive pressure gradient, $v = \partial\psi/\partial x$, on the upstream side of the topography, and a negative v on the downstream side. If these pressure gradients on each side were equal in strength, then the form drag would vanish as in the inviscid case. The presence of the positive vortex, on the downstream side of the hill, will increase the magnitude of v on that side relative to the upstream side. Thus, on multiplying v by h and integrating, the net effect is a negative form drag. The same analysis applies in the $\alpha = 0^\circ$ case (panel 3c). In both the $\alpha = -90^\circ$ case and the $\alpha = 0^\circ$ case, there is an enhanced gradient of pressure on the downstream side that accounts for the negative net form drag. In the $\alpha = -90^\circ$ case, this enhanced pressure gradient lies along the whole downstream side of the topography, while in the $\alpha = 0^\circ$ case, the region of enhanced pressure gradient is aligned perpendicular to the long topographic axis. The result is that so only a smaller portion of the region of enhanced pressure gradient effectively contributes to the form drag in the $\alpha = 0^\circ$ than in the $\alpha = -90^\circ$ case.

Now we turn to the question of why, in the weak topography case, the drag is stronger for the positive angle of attack than for the negative angle of the same magnitude. In the perturbation theory, we noted that the lowest order form drag does not have this asymmetry, and it is necessary to go to the next order to capture this effect. This higher order effect results from the nonlinear advection produced by the Jaco-

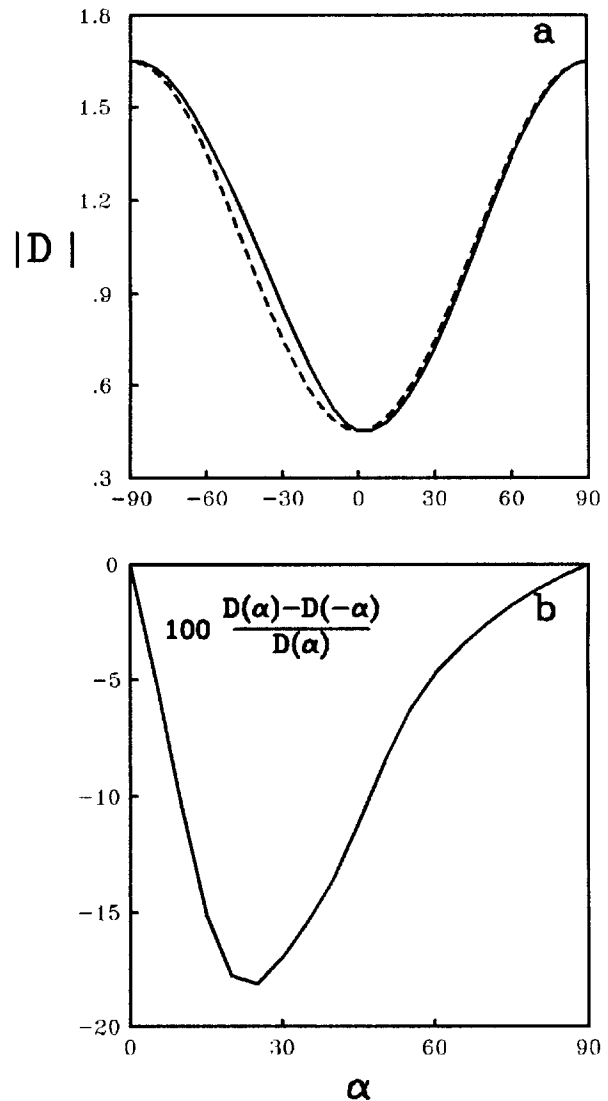


Figure 14. Form drag for the strong topography case, $h_0 = 100$. This data is taken from simulations using the code with spatial cutoff. (a) The absolute value of the stationary form drag is plotted as a function of attack angle. This is compared to the fit to the symmetric curve $A\sin^2(\alpha) + B\cos^2(\alpha)$ with A and B chosen to give a good fit at the extremal values of the data. (b) The relative variation of the difference between the drag at positive and negative angles of attack is plotted versus attack angle. Specifically the graph represents $100(D(\alpha) - D(-\alpha))/D(\alpha)$, where $D(\alpha)$ is the form drag for a given angle of attack, α .

bian, $J(\psi, h + \zeta)$. In the appendix, we show that the interaction, $J(\psi, h)$, does not contribute at the order of $D^{(3)}$ for elliptical topography. Thus it is only

through the vortex-vortex interaction, $J(\psi, \zeta)$, that $D^{(3)}$ contributes to the drag. Physically this term is related to the tendency of negative vorticity over the topography to displace the positive vortex in an arc in the clockwise direction about the center of the topography. In the $\alpha = -30^\circ$ case, in panel 3b, the negative vortex is displaced away from the crest of the topography and away from the region of negative vorticity. This results in a weaker induced pressure gradient compared to what it would have been without this angular displacement. In the $\alpha = +30^\circ$ case, in panel 3d, the negative vortex is displaced toward the crest of the topography and toward the region of negative vorticity. This results in a stronger induced pressure gradient compared to the lowest order case. Thus the form drag is stronger for the positive α case than for the negative α case. If we imagine steadily increasing α from $\alpha = -90$, we see the positive vortex first on the left side (looking upstream) of the crest of the topography, then at $\alpha = 0$ lying right over the crest, and then on the right side for $\alpha > 0$. Thus for $\alpha < 0$, the nonlinear advection displaces the negative vortex away from the topography, while for $\alpha > 0$ the displacement is toward the topography. This accounts for the result that the form drag is stronger for positive angles of attack than negative angles of the same size.

Given the above analysis for the weak topography case, how can we understand the transition to what we have called the strong topography regime in which the form drag is stronger for the negative angle of attack than for the positive angle? As noted above, this effect is not directly related to the formation of Taylor columns. Instead, the answer will be found in the relative positions of the vortices with respect to each other and to the topography. Figure 15 displays data gathered from a series of experiments representing topographies with amplitudes from $h_0 = 1$ to $h_0 = 50$, and to angles of attack $\alpha = \pm 30^\circ$. The positions of the peak of positive relative vorticity (triangles) and negative relative vorticity (dots) are shown over ellipses which represent the topography. First of all, note that for the $h_0 = 1$ case, the negative vortex peak is located almost directly over the center of the topography, and as h_0 increases, it is displaced along the crest, toward the nose of the topography in the $\alpha = +30^\circ$ case, but toward the tail in the $\alpha = -30^\circ$ case. For $h_0 = 1$, the positive peak vorticity is located slightly below the x -axis, directly downstream of the center of the topography. As h_0 increases, the displacement of the positive vorticity peak is rather

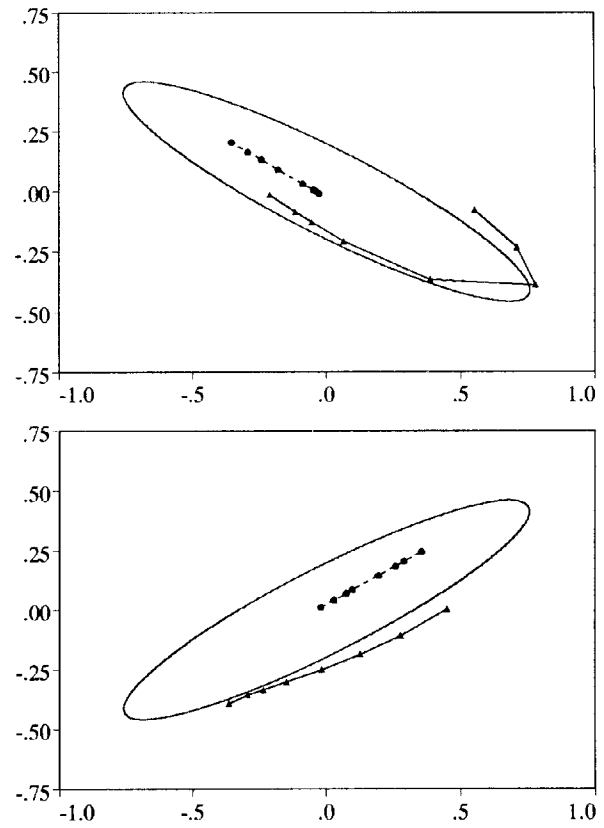


Figure 15. Positions of vorticity extrema for different values of the topographic height, h_0 . The flow is in the positive x -direction, and the orientation of the topography is indicated by the ellipses, with $\alpha = +30^\circ$ in panel (a) and $\alpha = -30^\circ$ in panel (b). The position of the positive (negative) vorticity peaks are indicated by the solid triangles (circles). The topographic heights represented are $h_0 = 1, 10, 15, 20, 25, 30, 40$, and 50 . In each panel, for $h_0 = 1$, the negative vortex is located approximately over the center of the ellipse, and the positive peak is just slightly below the x -axis, directly downstream of the center of the ellipse.

different for the two topographic orientations. For the $\alpha = -30^\circ$ case, the peak of positive vorticity simply moves further and further toward the nose of the topography but always remaining on the downstream side. For the $\alpha = +30^\circ$ case, the positive vorticity peak is displaced in an arc. Between $h_0 = 10$ and $h_0 = 15$, this peak crosses over the crest of the topography, moving from the downstream to the upstream side. From $h_0 = 15$ to $h_0 = 40$, the peak is displaced more and more toward the nose of the ellipse, remaining always on the upstream side. There then appears to be a discontinuous jump with a large displacement

putting the $h_0 = 50$ position back downstream but still on the upstream side of the ellipse. Actually this discontinuity in the graph is related to the fact that,

in the positive α cases, with very strong topography, there are two peaks of positive relative vorticity, as we can see in Figure 7d. Between $h_0 = 40$ and $h_0 = 50$ the trailing positive vorticity peak becomes stronger than the leading one, resulting in the jump in the graph in Figure 15a. The value of h_0 for which this jump occurs is also approximately the value of topography for which Taylor column formation first occurs. However, as we noted before, the transition to what we have called the strong topography regime occurs at the much smaller value of $h_0 \approx 15$. This shows that the relevant effect is that for $h_0 \approx 15$ the positive vortex peak crosses over from the trailing side of the topography to the leading side in the $\alpha = +30^\circ$ case, while no such transition occurs in the $\alpha = -30^\circ$ case.

We have found that a simple point vortex model based on the idea that it is the position of the positive vortex that determines whether we are in the strong or weak topographic regime can capture the transition between these regimes. Consider replacing the actual positive and negative vortices by two point vortices, one of each sign. Note that if the negative vortex was exactly at the center of the topography,

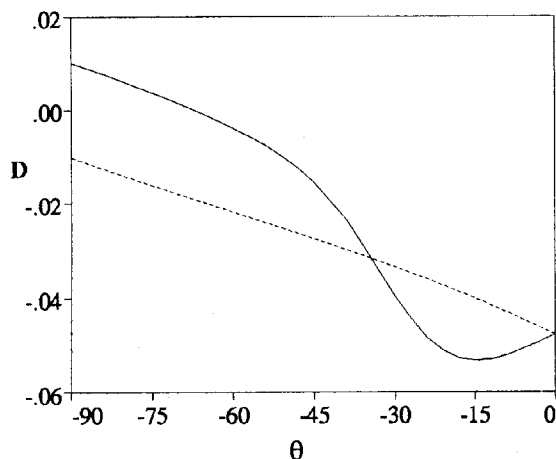


Figure 16. Drag due to a positive point vortex. The solid (dashed) curve shows the value of the drag, D , for the angle of attack $\alpha = +30^\circ$ ($\alpha = -30^\circ$). The drag is given as a function of the angular position, θ , measured from the positive x -axis, of the point vortex. The distance of the point vortex from the center of the topography has been fixed at $r_0 = 0.4$. The drag is normalized by $h_0\Gamma$, where h_0 is the topographic height and Γ is the strength of the point vortex.

then, by symmetry, it can have no contribution to the form drag. For topographic strengths less than $h_0 \approx 15$, the negative vortex is only displaced by a relatively small amount from the center of the topography; hence, as a first approximation, we neglect its contribution to the form drag and consider only the contribution coming from the positive vortex. Let us further assume that the only effect of increasing the strength of the topography is to change the angular position (θ measured from the x -axis) of the positive vortex. Accordingly, in the model, the positive vortex is taken to be a fixed distance r_0 from the center of the topography. Thus, we evaluate the contribution to the form drag from a point vortex placed in the position $(r_0 \cos \theta, r_0 \sin \theta)$ as a function of θ . The streamfunction for a point vortex of strength Γ at this position is given by

$$\psi = \frac{\Gamma}{2\pi} \ln(|\mathbf{r} - \mathbf{r}_0|). \quad (47)$$

The resulting form drag is

$$D = \frac{\Gamma}{2\pi} \int \int \frac{x - x_0}{|\mathbf{r} - \mathbf{r}_0|^2} h dx dy. \quad (48)$$

Performing the integration numerically, and varying only the angle θ , we obtain the plots shown in Figure 16. The solid graph is the drag, normalized by Γh_0 , for the topographic orientation $\alpha = +30^\circ$, and the dashed graph is for $\alpha = -30^\circ$. Keeping in mind that for this model the magnitude of the angle θ corresponds to the height of the topography, we note that for small θ the drag is stronger (i.e. more negative) for positive α than for negative α , and vice versa for large $|\theta|$. Thus, this point-vortex model does capture the same behavior, at least qualitatively, that we observed in the simulations. Here we have used $r_0 = 0.4$ in the calculations of the drag. The angle θ at which the model passes from the weak to the strong regime is about $\theta = -30^\circ$, which corresponds to placing the point vortex right over the crest of the topography. However, the cross-over point does depend somewhat on the value chosen for r_0 . Furthermore, note that as the angle θ becomes very large, a point will be reached at which the point vortex contributes positively to the form drag, as may be intuitively obvious. But, of course, the total drag must be negative, so it is clear that for very large displacements, θ , the contribution of the negative vortex cannot be neglected. To properly capture all aspects of the dependence of form drag on topographic orientation and height would require a far more elaborate model than

our one point model. Nevertheless, this model does capture the essential feature of the form drag's asymmetric dependence on the sign of α in the weak and strong topography regimes.

Conclusion

We have explored how the drag that an elongated hill exerts on a flow, in a rotating fluid, depends on the orientation of that hill with respect to the flow direction. As might be expected intuitively, the drag is strongest when the hill's long axis is perpendicular to the flow direction, and it is least when that axis is parallel to the flow. A somewhat less intuitive result was that the strength of the form drag, even for hills with a horizontal cross section which is symmetric about its long axis, depends not only on the size of the "angle of attack," but also on the sign of that angle. We related this asymmetric dependence on angle to an interaction between the basic asymmetry in the mechanism of vortex tube compression and the breaking of the circular symmetry of the topography. The advection of zero relative vorticity fluid up onto the topography always results in an anticyclone over the topography and this tends to shift the downstream cyclone in an anticyclonic direction, which puts the cyclone either closer to or further from the topography depending on the topographic shape and orientation. Whether a positive angle of orientation results in more or less drag than the corresponding negative angle depends on the height of the hill. We defined a weak and strong (i.e., low and high) topography regime. For weak topography, the drag is stronger for a positive angle of attack than for an angle of the same size but opposite sign. For strong topography, this relationship is reversed, with the negative angle of attack giving the stronger form drag. It is often convenient to associate Taylor column formation with a strong topographic regime. However, in this study, we found that the formation of Taylor columns did not signal the transition from the qualitatively different behaviors of the form drag in the weak and strong regimes. Rather, we found that these regimes were defined by the qualitatively different distributions of vorticity over the topography. The weak topography regime corresponds to the case in which the positive vortex is located on the downstream side of the topography for *both* the positive and negative angle of attack, while, in the strong topography regime, the positive vortex is on the downstream side for the negative angle of attack, and on the upstream side for the positive angle of attack. We also provided a simple

point-vortex model which captures these same effects.

In these studies, we have explored a wide range of values of the topographic height. The values of the viscosity were also varied in test cases designed simply to insure that the phenomena reported do exist over a range of over an order of magnitude in each direction for ν and τ . There are, of course, many other physical effects that we have not included in the simple model used here, and some of these could modify our results. Perhaps the most interesting effects to consider would be those that would allow the propagation of waves. Recall that, as we noted above, in the absence of viscosity, in our simple model, the inviscid stationary flow suffers no form drag due to the presence of the hill, a manifestation of D'Alembert's paradox. However, the possibility of radiating energy infinitely far away, allows for a finite drag even in the inviscid case (see Batchelor, 1967). Two very natural candidates for such radiation would be Rossby waves and internal gravity waves. Rossby waves will result either from a large-scale bottom slope or a variation of rotation rate with latitude. Internal gravity waves require density stratification.

Acknowledgments

This research has been supported in part by Office of Naval Research grant N00014-93-1-0459 and by National Science Foundation grant OCE 91-21998. R.P. thanks the Progetto Nazionale Ricerche in Antartide (PNRA) and the Physics Committee of the National Research Council (CNR) for providing financial support for this study. The numerical simulations were performed at the San Diego Super Computer Center. We are grateful for helpful discussions with William Young.

References

- Bannon, P.R. 1980: Rotating barotropic flow over finite isolated topography. *J. Fluid Mech.* **101**, 281-306.
- Bannon, P.R. 1985: Flow acceleration and mountain drag. *J. Atmos. Sci.* **42**, 2445-2453.
- Batchelor, G.K. 1967: *An Introduction to Fluid Dynamics*. Cambridge University Press.
- Boyer, D.L. 1971: Rotating flow over long shallow ridges. *Geophys. Fluid Dyn.* **2**, 165-183.
- Carnevale G.F. and Frederiksen J.S. 1987: Nonlinear Stability and Statistical Mechanics of Flow over Topography. *J. Fluid Mech.* **175**, 157-181.

- Carnevale G.F., Purini R., Orlandi P., and Cavazza P. 1995: Barotropic quasi-geostrophic f-plane flow over anisotropic topography. *J. Fluid Mech.* **285**, 329-347.
- Cook, K.H. and Held, I.M. 1992: The stationary response to large-scale orography in a general circulation model and a linear model. *J. Atmos. Sci.* **49**, 525-539.
- Genin, A. 1987: Effects of seamount topography and currents on biological processes, Thesis, University of California, San Diego.
- Genin, A., Noble M. and Lonsdale P.F. 1989: Tidal currents and anticyclonic motions on two North Pacific seamounts, *Deep-Sea Research* **36**, 1803-1815.
- Hart, J.E. 1979: Barotropic quasi-geostrophic flow over anisotropic mountains, *J. Atmos. Sci.* **36**, 1736-1746.
- Huppert, H.E. and Bryan, K. 1976: Topographically generated eddies. *Deep-Sea Res.* **23**, 655-679.
- Johnson, E.R. 1978: Trapped vortices in rotating flow. *J. Fluid Mech.* **86**, 209-224.
- Merkine, L. and Kalnay-Rivas, E. 1976: Rotating stratified flow over finite isolated topography. *J. Atmos. Sci.* **33**, 908-922.
- McWilliams J.C., Holland W.R., and Chow J. 1978: A description of numerical Antarctic circumpolar currents, *Dyn. Atmos. Oceans* **2**, 213-291.
- Orlanski I. 1976: A simple boundary condition for unbounded hyperbolic flows. *J. Comp. Phys.* **21**, 251-269.
- Patterson, G.S. & Orszag, S.A. 1972: Spectral calculations of isotropic turbulence, efficient removal of aliasing interactions. *Phys. Fluids* **14**, 2538-2541.
- Pedlosky, J. 1987: *Geophysical Fluid Dynamics*. New York: Springer-Verlag. 2nd ed.
- Pierrehumbert, R.T. and Malguzzi, P. 1984: Forced coherent structures and local multiple equilibria in a barotropic atmosphere. *J. Atmos. Sci.* **41**, 246-257.
- Treguier A.M. and McWilliams J.C. 1990: Topographic influence on wind-driven, stratified flow in a β -channel: an idealized model for the Antarctic Circumpolar Current, *J. Phys. Ocean.*, **20**, 321-343.
- Verron J. and Le Provost C. 1985: A numerical study of quasi-geostrophic flow over isolated topography, *J. Fluid Mech.* **154**, 231-252.
- Wolff J-O. and Olbers D.J. 1989: The dynamical balance of the Antarctic Circumpolar Current studied with an eddy resolving quasi-geostrophic model, in *Mesoscale/Synoptic Coherent Structures in Geophysical Turbulence*, pp. 181-195 Ed's. J.C.J. Nihoul and B.M. Jamart (Elsevier, Amsterdam).
- Wolff J-O., Meier-Reimer E., and Olbers D.J. 1991: Wind-Driven Flow over Topography in a zonal β -plane channel: a quasi-geostrophic model of the Antarctic Circumpolar Current. *J. Phys. Ocean.* **21**, 236-264.

Appendix: calculation of $D^{(3)}$

The basis for small topography perturbation theory was developed in equations (24)-(35). Since the drag,

$$D = \int h \frac{\partial \psi}{\partial x} dx dy = - \int \frac{ik_x}{k^2} \zeta_{\mathbf{k}} h_{-\mathbf{k}} \frac{d^2 k}{(2\pi)^2},$$

explicitly contains the topography to the first power, and since the vorticity,

$$\zeta = \zeta^{(1)} + \zeta^{(2)} + \zeta^{(3)} + \dots,$$

is at lowest order proportional to the topography, it follows that the lowest order contribution to the form drag, as given in (35), denoted by $D^{(2)}$, is second order in the topography. The next order term $D^{(3)}$ is given by

$$D^{(3)} = - \int \frac{ik_x}{k^2} \zeta_{\mathbf{k}}^{(2)} h_{-\mathbf{k}} \frac{d^2 k}{(2\pi)^2}, \quad (\text{A1})$$

and since

$$\zeta_{\mathbf{k}}^{(2)} = -g_{\mathbf{k}} J_{\mathbf{k}}(\psi^{(1)}, \zeta^{(1)} + h), \quad (\text{30})$$

this is the lowest order term to involve the nonlinear self-advection. The Fourier transform of the Jacobian can be represented as

$$J_{\mathbf{k}}(A, B) = \int e^{-i\mathbf{k} \cdot \mathbf{r}} \left(\frac{\partial A}{\partial x} \frac{\partial B}{\partial y} - \frac{\partial A}{\partial y} \frac{\partial B}{\partial x} \right) d^2 r \quad (\text{A2})$$

$$= - \int e^{i(-\mathbf{k} \cdot \mathbf{r} + \mathbf{p} \cdot \mathbf{r} + \mathbf{q} \cdot \mathbf{r})} (p_x q_y - p_y q_x)$$

$$\times A_{\mathbf{p}} B_{\mathbf{q}} d^2 r \frac{d^2 p}{(2\pi)^2} \frac{d^2 q}{(2\pi)^2}$$

$$= - \int \hat{\mathbf{z}} \cdot \mathbf{p} \times \mathbf{q} A_{\mathbf{p}} B_{\mathbf{q}} (2\pi)^2 \delta(-\mathbf{k} + \mathbf{p} + \mathbf{q}) \frac{d^2 p}{(2\pi)^2} \frac{d^2 q}{(2\pi)^2},$$

where $\hat{\mathbf{z}} \cdot \mathbf{p} \times \mathbf{q} = (p_x q_y - p_y q_x)$ and $\delta(\cdot)$ is the multi-dimensional Dirac delta function.

Now we can calculate the $D^{(3)}$ term. Begin by changing the sign of the dummy integration variable, \mathbf{k} , in (A1), and substituting for $\zeta^{(2)}$ from (30) to obtain

$$D^{(3)} = D_{\psi, h}^{(3)} + D_{\psi, \zeta}^{(3)} \\ = - \int \frac{ik_x}{k^2} g_{-\mathbf{k}} J_{-\mathbf{k}}(\psi^{(1)}, \zeta^{(1)} + h) h_{\mathbf{k}} \frac{d^2 k}{(2\pi)^2}.$$

Here we consider the two components, $D_{\psi, h}^{(3)}$ and $D_{\psi, \zeta}^{(3)}$, which correspond to vortex-topography and vortex-vortex interactions separately. After introducing the

expression for $J_{\mathbf{k}}$ and the definition (28) for the linear Green's function, we obtain, for the vortex-topography contribution, the result

$$D_{\psi,h}^{(3)} = I_1 = -U \int \frac{k_x p_x}{k^2 p^2} g_{-\mathbf{k}} g_{\mathbf{p}} h_{\mathbf{k}} h_{\mathbf{p}} h_{\mathbf{q}} \mathcal{D}_{\mathbf{k}\mathbf{p}\mathbf{q}} \quad (\text{A3})$$

$$= -U \int k_x p_x [(k_x p_x U^2 + d_k d_p) + iU(k_x d_p - p_x d_k)] \times b_{\mathbf{k}} b_{\mathbf{p}} h_{\mathbf{q}} \mathcal{D}_{\mathbf{k}\mathbf{p}\mathbf{q}}, \quad (\text{A4})$$

where

$$\mathcal{D}_{\mathbf{k}\mathbf{p}\mathbf{q}} \equiv (\hat{\mathbf{z}} \cdot \mathbf{p} \times \mathbf{q}) \times (2\pi)^2 \delta(\mathbf{k} + \mathbf{p} + \mathbf{q}) \frac{d^2 k}{(2\pi)^2} \frac{d^2 p}{(2\pi)^2} \frac{d^2 q}{(2\pi)^2}, \quad (\text{A6})$$

and

$$b_{\mathbf{k}} \equiv \frac{h_{\mathbf{k}}}{k^2 (U^2 k_x^2 + d_k^2)}. \quad (\text{A5})$$

Note that since the Dirac delta function forces $\mathbf{k} + \mathbf{p} + \mathbf{q} = 0$, it follows that $\mathbf{k} \times \mathbf{p} = -\mathbf{k} \times \mathbf{q} = \mathbf{q} \times \mathbf{k}$, and so $\mathcal{D}_{\mathbf{k}\mathbf{p}\mathbf{q}}$ is symmetric under cyclic permutation of the wavevectors $\{\mathbf{k}, \mathbf{p}, \mathbf{q}\}$, and it is antisymmetric under their pairwise interchange.

The first term in the integrand of the integral $D_{\psi,h}^{(3)} = I_1$ integrates to zero. To see this, note that this term is antisymmetric under the interchange of the dummy variables \mathbf{k} and \mathbf{p} , since $\mathcal{D}_{\mathbf{k}\mathbf{p}\mathbf{q}} = -\mathcal{D}_{\mathbf{p}\mathbf{k}\mathbf{q}}$ while the rest of the factors are symmetric in these variables. Subsequently, integration over \mathbf{k} and \mathbf{p} eliminates this antisymmetric term, leaving

$$I_1 = -iU^2 \int k_x p_x (k_x d_p - p_x d_k) b_{\mathbf{k}} b_{\mathbf{p}} h_{\mathbf{q}} \mathcal{D}_{\mathbf{k}\mathbf{p}\mathbf{q}} \quad (\text{A5})$$

In general, I_1 need not vanish; however, it will vanish if the topography has the point reflection symmetry, $h(x, y) = h(-x, -y)$, as is the case for our elliptical topography. The point reflection symmetry implies $h_{\mathbf{k}} = h_{-\mathbf{k}}$. If the topography has this symmetry, then changing the signs of all three wavevectors of integration changes the sign of the integrand (note $\mathcal{D}_{\mathbf{k}\mathbf{p}\mathbf{q}} = \mathcal{D}_{-\mathbf{k}, -\mathbf{p}, -\mathbf{q}}$). Thus, the vortex-topography interaction contributes to the form drag, $D^{(3)}$ only if the topography does not have point reflection symmetry.

Next we turn to the vortex-vortex interaction. For this we have

$$D_{\psi,\zeta}^{(3)} = -U \int \frac{k_x p_x}{k^2 p^2} g_{-\mathbf{k}} g_{\mathbf{p}} h_{\mathbf{k}} h_{\mathbf{p}} h_{\mathbf{q}} (-iq_x U g_{\mathbf{q}}) \mathcal{D}_{\mathbf{k}\mathbf{p}\mathbf{q}} \quad (\text{A6})$$

$$= -U \int k_x p_x [(k_x p_x U^2 + d_k d_p) + iU(k_x d_p - p_x d_k)] \times (-\frac{iq_x U(-iq_x + d_q)}{(q_x^2 U^2 + d_q^2)}) b_{\mathbf{k}} b_{\mathbf{p}} h_{\mathbf{q}} \mathcal{D}_{\mathbf{k}\mathbf{p}\mathbf{q}}. \quad (\text{A7})$$

Expanding this integral further leads to an integrand containing several terms, but most of these can be shown to vanish by using the symmetry properties of $\mathcal{D}_{\mathbf{k}\mathbf{p}\mathbf{q}}$. There are five different kinds of terms which appear in the expansion. We will name these I_i for $i=2-6$, and discuss each separately.

The next integral to consider is

$$I_2 = iU^2 \int q^2 k_x p_x q_x d_k d_p d_q b_{\mathbf{k}} b_{\mathbf{p}} b_{\mathbf{q}} \mathcal{D}_{\mathbf{k}\mathbf{p}\mathbf{q}}. \quad (\text{A8})$$

This integral vanishes for any topography. To demonstrate this, we first note that the fact that $\mathcal{D}_{\mathbf{k}\mathbf{p}\mathbf{q}} = -\mathcal{D}_{\mathbf{k}\mathbf{q}\mathbf{p}}$ allows us to write

$$I_2 = \frac{i}{2} U^2 \int (q^2 - p^2) k_x p_x q_x d_k d_p d_q b_{\mathbf{k}} b_{\mathbf{p}} b_{\mathbf{q}} \mathcal{D}_{\mathbf{k}\mathbf{p}\mathbf{q}}. \quad (\text{A9})$$

Then, by using the cyclic permutation symmetry of $\mathcal{D}_{\mathbf{k}\mathbf{p}\mathbf{q}}$, we obtain

$$I_2 = \frac{i}{6} U^2 \int [(q^2 - p^2) + (k^2 - p^2) + (p^2 - q^2)] \times k_x p_x q_x d_k d_p d_q b_{\mathbf{k}} b_{\mathbf{p}} b_{\mathbf{q}} \mathcal{D}_{\mathbf{k}\mathbf{p}\mathbf{q}}. \quad (\text{A10})$$

This last expression is seen to vanish identically on noting that the terms within the square brackets sum to zero.

The next contribution is the integral

$$I_3 = iU^4 \int q^2 d_q k_x^2 p_x^2 q_x b_{\mathbf{k}} b_{\mathbf{p}} b_{\mathbf{q}} \mathcal{D}_{\mathbf{k}\mathbf{p}\mathbf{q}}. \quad (\text{A11})$$

This integral also vanishes for all topography as can be seen by interchanging the dummy variable \mathbf{k} and \mathbf{p} and noting that the integrand then reverses sign.

Continuing, we have

$$I_4 = iU^4 \int q^2 (k_x d_p q_x - p_x q_x d_k) k_x p_x q_x b_{\mathbf{k}} b_{\mathbf{p}} b_{\mathbf{q}} \mathcal{D}_{\mathbf{k}\mathbf{p}\mathbf{q}}. \quad (\text{A12})$$

This expression can be simplified by interchanging \mathbf{k} and \mathbf{p} in the second term in the integrand and then adding the result to the first term. Thus

$$I_4 = 2iU^4 \int q^2 d_p k_x^2 p_x q_x^2 b_k b_p b_q \mathcal{D}_{\mathbf{k}\mathbf{p}\mathbf{q}}.$$

As in the case of I_1 , the resulting integral vanishes if $h_{\mathbf{k}} = h_{-\mathbf{k}}$. This can be seen by noting that the changing the signs of all three wavevectors of integration simply changes the sign of the integrand. Thus I_4 only contributes to the form drag if the topography does not have point reflection symmetry.

The next integral is

$$I_5 = U^5 \int q^2 k_x^2 p_x^2 q_x^2 b_k b_p b_q \mathcal{D}_{\mathbf{k}\mathbf{p}\mathbf{q}}. \quad (\text{A13})$$

We can see that this integral vanishes for all topography by using the same steps that we used in the case of I_2 .

The final integral is

$$I_6 = -U^3 \int q^2 (k_x d_p d_q - p_x d_q d_k - q_x d_k d_p) \\ \times k_x p_x q_x b_k b_p b_q \mathcal{D}_{\mathbf{k}\mathbf{p}\mathbf{q}}. \quad (\text{A14})$$

The third term in the parentheses will not contribute to the integral since for that term the integrand is antisymmetric under interchange of \mathbf{k} and \mathbf{p} . Then by interchanging \mathbf{k} and \mathbf{p} in the second term in the integrand, we obtain

$$I_6 = -2U^3 \int q^2 k_x d_p d_q k_x p_x q_x b_k b_p b_q \mathcal{D}_{\mathbf{k}\mathbf{p}\mathbf{q}} \quad (\text{A15})$$

Even for topography with point reflection symmetry, this term need not vanish. Hence it is the only third order term that will contribute in the case of our elliptical topography.

To summarize, we have shown that in general $D^{(3)} = I_1 + I_4 + I_6$, but in the case of topography with point reflection symmetry, as is the case of the elliptical topography, both I_1 and I_4 vanish. Also we have shown that for elliptically symmetric topography, there is no contribution to $D^{(3)}$ directly from the vortex-topography interaction, except indirectly through the vortex-vortex interaction.